



Article

Process-Structure-Property Interdependencies in Non-Isothermal Powder Bed Fusion of Polyamide 12

Samuel Schlicht ^{1,2,*} , Simon Cholewa ^{1,2} and Dietmar Drummer ^{1,2}

¹ Institute of Polymer Technology, Friedrich-Alexander-Universität Erlangen-Nürnberg, Am Weichselgarten 10, 91058 Erlangen, Germany

² Collaborative Research Center 814, Friedrich-Alexander-Universität Erlangen-Nürnberg, Am Weichselgarten 10, 91058 Erlangen, Germany

* Correspondence: samuel.schlicht@fau.de

Abstract: Non-isothermal laser-based powder bed fusion (LPBF) of polymers suggests the potential for significantly extending the range of materials applicable for powder-based additive manufacturing of polymers, relying on the absence of a material-specific processing window. To allow for the support-free manufacturing of polymers at a build chamber temperature of 25 °C, applied processing strategies comprise the combination of fractal exposure strategies and locally quasi-simultaneous exposure of distinct segments of a particular cross section for minimizing crystallization-induced part deflection. Based on the parameter-dependent control of emerging cooling rates, formed part morphologies and resulting mechanical properties can be modified. Thermographic in situ measurements allow for correlating thermal processing conditions and crystallization kinetics with component-specific mechanical, morphological, and microstructural properties, assessed ex situ. Part morphologies formed at crystallization temperatures below 70 °C, induced by reduced laser exposure times, are characterized by a nano-spherulitic structure, exhibiting an enhanced elongation at break. An ambient temperature of 25 °C is associated with the predominant formation of a combined ($\alpha + \gamma$)-phase, induced by the rapid cooling and subsequent laser-induced tempering of distinct layers, yielding a periodic microstructural evolution. The presented results demonstrate a novel approach for obtaining nano-spherulitic morphologies, enabling the exposure-based targeted adaption of morphological properties. Furthermore, the thermographic inline assessment of crystallization kinetics allows for the enhanced understanding of process-morphology interdependencies in laser-based manufacturing processes of semi-crystalline polymers.

Keywords: non-isothermal; powder bed fusion; laser sintering; low temperature powder bed fusion; polyamide 12



Citation: Schlicht, S.; Cholewa, S.; Drummer, D. Process-Structure-Property Interdependencies in Non-Isothermal Powder Bed Fusion of Polyamide 12. *J. Manuf. Mater. Process.* **2023**, *7*, 33. <https://doi.org/10.3390/jmmp7010033>

Academic Editor: Prashanth Konda Gokuldoss

Received: 10 January 2023
Revised: 24 January 2023
Accepted: 28 January 2023
Published: 30 January 2023



Copyright: © 2023 by the authors. Licensee MDPI, Basel, Switzerland. This article is an open access article distributed under the terms and conditions of the Creative Commons Attribution (CC BY) license (<https://creativecommons.org/licenses/by/4.0/>).

1. Introduction

Laser-based powder bed fusion (LPBF) of polymers is a powder-based additive manufacturing process that allows for the fabrication of dense components with high mechanical properties. The present predominant application of quasi-isothermal processing is subject to a broad range of constraints, governed by the accordance of applied thermal boundary conditions and the isothermal processing window of semi-crystalline polymers. The required continuous heating of the powder bed surface is associated with considerable thermal material aging [1,2], inherently restricting the manufacturing of thermo-sensitive material systems and limiting the recyclability of applied powders [1]. Furthermore, the inherent requirement for a thermal processing window implicitly impairs the processing of modified thermoplastics with implicitly adapted crystallization kinetics, such as highly filled systems [3], hence indicating the requirement for novel processing strategies.

In contrast to established quasi-isothermal processing, non-isothermal processing of polymers allows for a significant adaption of formed morphologies, exhibiting significantly

reduced spherulite sizes [4–6] and adapted thermal material properties [4] of produced parts. Based on the inherently increased cooling rate, occurring subsequent to the exposure step [4], varied mechanical properties are described based on the application of support structures to avoid part warpage [6], correlated with the aforementioned micro-spherulitic morphology. The avoidance of support structures for considerably improving the technological and economic viability of non-isothermal LPBF is described based on applying fractal, quasi-simultaneous exposure strategies [4]. The spatial and temporal discretization of the exposure step allows for the explicit specification of temporal boundary conditions, such as the exposure time, that are described to significantly influence part properties in quasi-isothermal processing [7].

Since non-isothermal processing differs significantly from quasi-isothermal processing in terms of altered mechanisms governing the evolution of the microstructure, there is a lack of information regarding the effects of the process on both the microstructure and the resulting mechanical properties. Therefore, exploiting the technological potential of non-isothermal polymer-based LPBF requires a holistic understanding of the dependencies of formed micro- and macroscopic properties on the underlying process to enable the process-based in situ modification of formed microstructures and resulting component properties.

2. State of the Art

2.1. Exposure-Dependent Temperature Fields in Laser-Based Powder Bed Fusion

Constituting a decisive factor in laser-based additive manufacturing processes, the laser exposure process has been approached based on thermographic in situ investigations [8,9], numerical simulations [10] and with regard to resulting part properties [11]. Established exposure strategies predominantly rely on linear exposure vectors, being associated with an inherent dependence of resulting temperature fields on the underlying exposed geometry observed for quasi-isothermal processing [8,9]. Geometry-dependent effects are interlinked to a varying extent of heat accumulation [12–14], affecting resulting peak temperatures and corresponding residual stresses in LPBF of metal alloys. For minimizing the occurrence of residual stresses and associated stress cracking, segmented exposure strategies have been introduced [10,15–17] and have since gained practical relevance. Based on numerical investigations [16], a positive correlation of the underlying exposure vector length and the formation of residual stresses is described, indicating a structural geometry-dependency of corresponding temperature fields. Extending the concept of segmented exposure strategies, Catchpole-Smith et al. (2016) [17] described the application of the fractal Hilbert curve for the additive manufacturing of nickel-base alloys, considerably reducing the extent of stress cracking. In addition to minimizing residual stresses, fractal space-filling curves were shown to promote the formation of geometry-independent temperature fields [18], hence limiting the influence of heat accumulation on the thermal history of a specific cross section.

2.2. Thermal Processing Conditions in Powder Bed Fusion of Polymers

Following the state of the art, LPBF predominantly relies on the quasi-isothermal processing of semi-crystalline thermoplastics. In contrast to the idealized model of isothermal processing, recent research has queried the isothermal assumption and the inherent avoidance of crystallization during the build process. Based on qualitatively assessing the mechanical resistance of produced parts, Drummer et al. (2019) [19] characterized the crystallization of the polymer melt in situ, indicating the accelerated crystallization of the molten component under process-related conditions. Based on numerical approaches, Soldner et al. [20,21] characterized the interdependence of geometric boundary conditions and isothermal crystallization kinetics, observing a spatially heterogeneous crystallization of parts. The crystallization kinetics of polyamide 12 have been investigated with regard to temperature-dependent isothermal [22–25] and cooling rate dependent non-isothermal [22,26–28] crystallization, identifying the influence of varying thermal boundary conditions on crystallization kinetics [24] occurring in quasi-isothermal LPBF of PA12. Shen

et al. (2021) [29] applied numerical approaches for determining the influence of thermal boundary conditions on the emergence of residual stresses in LPBF. In accordance with experimental investigations, numerical modeling displays a significantly accelerated material crystallization induced by elevated cooling rates, correlated with an increased level of residual stress [29]. In contrast to quasi-isothermal processing, prevailing in academia and industry, Niino et al. (2011) [6,30] employed considerably reduced build chamber temperatures by using support structures similar to metal-based LPBF, obtaining considerably altered morphological properties and enhanced failure properties [6].

2.3. Process Influences of Non-Isothermal Crystallization Properties of Polyamide 12

The understanding of non-isothermal crystallization of applied materials is essential for considering both process-specific effects and interdependencies on resulting component properties in LPBF. Due to the widespread application of PA12 in LPBF, recent research has focused on both isothermal [22,24,31] and non-isothermal crystallization properties [26,27,31] of polyamide 12. In contrast to quasi-isothermal processing of PA12, a complex interdependency of the material aging state [23], underlying cooling rates, emerging nucleation mechanisms [27], and resulting material phases [22] is observed under non-isothermal conditions. With regard to non-isothermal crystallization kinetics, the Nakamura model [32,33] is widely applied to empirically describe the non-isothermal crystallization of PA12 for analytical purposes [24,31] and for process simulations [21]. Non-isothermal crystallization of PA12 is predominantly governed by the temperature-dependent formation of distinct material phases [22]. Slow non-isothermal cooling of PA12 at atmospheric conditions yields the stable γ -phase [22]. In contrast, mesomorphic structures are obtained by fast cooling, e.g., quenching, from the melt. The mesomorphic phase undergoes an irreversible phase transformation into the γ -phase among heating, implying the significance of multiple exposure- and cooling-induced phase changes in non-isothermal, laser-based additive manufacturing. The formation of the mesomorphic phase has been described to occur at crystallization temperatures close to the glass transition temperature [22], indicating an implicit influence of thermal boundary conditions and corresponding processing parameters on the resulting phase composition.

With regard to formed spherulitic structures, Plummer et al. (2001) described the positive relationship between the underlying isothermal crystallization temperature and the corresponding spherulite radius and the lamellar thickness [34], consistent with the intra-layer dependency of formed microspherulitic structures in non-isothermal laser melting of polyamide 12 [4,6]. The formation of nano- and microspherulitic structures, described in the recent literature, suggests implications for corresponding mechanical properties due to the negative correlation of observed spherulite diameters and the elongation at break, described for the application of isotactic polypropylene [35].

3. Methodology

3.1. Implementation of Non-Isothermal Processing Strategies

The combination of a fractal exposure path generation conducted with iterative programming, and the repetitive, quasi-simultaneous exposure of different segments, as described by Schlicht et al. (2022) [4], represents the foundation for the non-isothermal, support-free processing of polymers. By applying a constant laser power of $P = 2.5$ W and an exposure speed of $v = 500$ mm s⁻¹, the resulting energy density was implicitly specified based on a varied quasi-simultaneous exposure time that defines the cumulative exposure time of distinct, consecutively exposed segments. Underlying segments depict a structural anisotropy, influenced by the specified segment size of 1×2.5 mm². The applied exposure structure of distinct segments is displayed in Figure 1, resembling a closed segment of the space-filling Peano curve [36]. To allow for the exposure of thin-walled geometries, distinct sub-segments were trimmed according to the underlying geometry using previously applied methodologies [4], applying an algorithm proposed by Yang et al. (2003) [37] for adapting space-filling, fractal curves to any geometry.

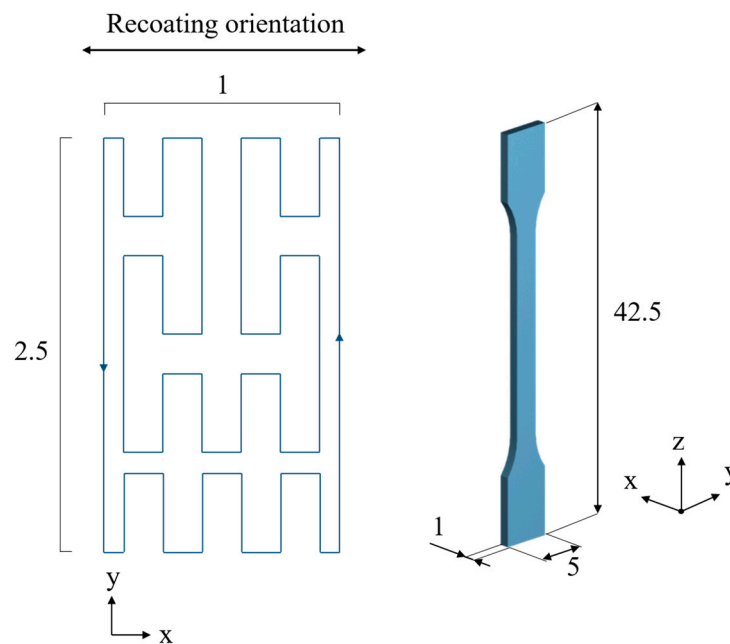


Figure 1. Depiction of the applied exposure paths of quasi-simultaneously exposed segments and the corresponding part orientation.

3.2. Materials and Processing

Considering the predominant application in quasi-isothermal processing of polymers, commercially available polyamide 12 was applied as the underlying material. A polyamide 12 powder of type PA 2200, EOS GmbH, Krailling, Germany, was used as received, exhibiting a melting point of $T_{Melting} = 184 \text{ }^\circ\text{C}$, assessed by means of differential scanning calorimetry ($dT/dt = 10 \text{ K min}^{-1}$). To allow for the implementation of quasi-simultaneous, fractal exposure strategies, a freely configurable research system, described by Drummer et al. (2019) [19], was used. By applying a fixed optical setup, a constant laser spot diameter of $d = 0.5 \text{ mm}$ ($I = 1/e^2$) was employed. To allow for the process-integrated assessment of temperature fields, thermal imaging was conducted, using a thermographic camera of type IRCAM VELOX 1310k SM (IRCAM GmbH, Erlangen, Germany), covering a spectral range from $\lambda = 1.5$ to $5.5 \text{ }\mu\text{m}$. Based on a fixed working distance, a constant spatial and temporal resolution of $140 \times 140 \text{ }\mu\text{m}^2$ and $f = 355 \text{ Hz}$, respectively, were specified. Thermal process characteristics were determined applying an emission coefficient of $\epsilon = 0.9$ [8].

3.3. Design of Experiments

To determine the influence of varied processing parameters on morphological and mechanical characteristics, the underlying quasi-simultaneous, segment-specific exposure time was varied in discrete steps, displayed in Table 1.

Table 1. Overview of applied quasi-simultaneous exposure parameters.

Quasi-Simultaneous Exposure Time/s	Segment Specific Energy Input/J
0.350	0.875
0.364	0.910
0.378	0.945
0.392	0.980
0.406	1.015
0.420	1.050
0.434	1.085

Further processing parameters include a build temperature of $T_B = 25\text{ }^\circ\text{C}$, a recoating speed of $v = 125\text{ mm s}^{-1}$ and a layer height of $h_{\text{Layer}} = 100\text{ }\mu\text{m}$. Manufactured specimens comprise scaled, thin-walled tensile bars designed according to ISO 3167, type 1A. For resembling thin-walled geometries, an isotropic scale factor of 0.25 was applied to the standardized geometry, corresponding to a constant wall thickness of 1.0 mm. Given the upward build orientation, a minimum rectangular cross section of 2.5 mm^2 was obtained, corresponding to the exposure of a single sub-segment. A number of $n = 5$ specimens, corresponding to a specific parameter set, were manufactured.

3.4. Mechanical and Microstructural Characterization

Quasi-static mechanical characterizations of manufactured tensile specimens were conducted on a tensile testing machine of type Instron 5968, Illinois Tool Works Inc., Norwood, MA, based on ISO 527-2, applying strain rates of $ds/dt = 0.25\text{ mm min}^{-1}$ and $ds/dt = 1.25\text{ mm min}^{-1}$ to evaluate the elastic modulus and to determine the ultimate tensile strength. To allow for the assessment of temperature-dependent dynamic mechanical properties, dynamic mechanical tensile testing was conducted using a solid analyzer of type RSA-G2, TA Instruments, New Castle, DE, USA, applying a heating rate of $dT/dt = 2\text{ K min}^{-1}$, an oscillation strain of 0.02%, and a frequency of $f = 1\text{ Hz}$. Complementary microstructural characterizations are based on polarized light microscopy of prepared thin-cuts, conducted using a Carl Zeiss AxioImager 2, Carl Zeiss Microscopy Deutschland GmbH, Oberkochen, Germany. For characterizing the surface topology of manufactured specimens, laser scanning microscopy is conducted using a microscope of type VK-X1000, Keyence Corporation, Osaka, Japan. Computed tomographic investigations of manufactured specimens are based on applying a sub- μ -CT (Fraunhofer Institute for Integrated Circuits (IIS) e.V., Erlangen, Germany), yielding an isotropic spatial resolution of $4\text{ }\mu\text{m}$. Subsequent analytical investigations of the spatial distribution of detected pores rely on the automated analysis of three-dimensional density distributions.

3.5. Thermal Characterization

Fast scanning calorimetry (FSC) was used for the process-related characterization of temperature-dependent crystallization kinetics, considering noticeably increased cooling rates in non-isothermal processing of polymers. The underlying experimental studies, which make use of a chip calorimeter of the type Flash DSC 2+ (Mettler-Toledo GmbH, Giessen, Germany), comprised both non-isothermal and isothermal characterizations for obtaining comparative crystallization kinetics under varying cooling kinetics. Applied temperature–time profiles are schematically displayed in Figure 2, illustrating the application of constant cooling rates suitable for non-isothermal fast scanning calorimetry.

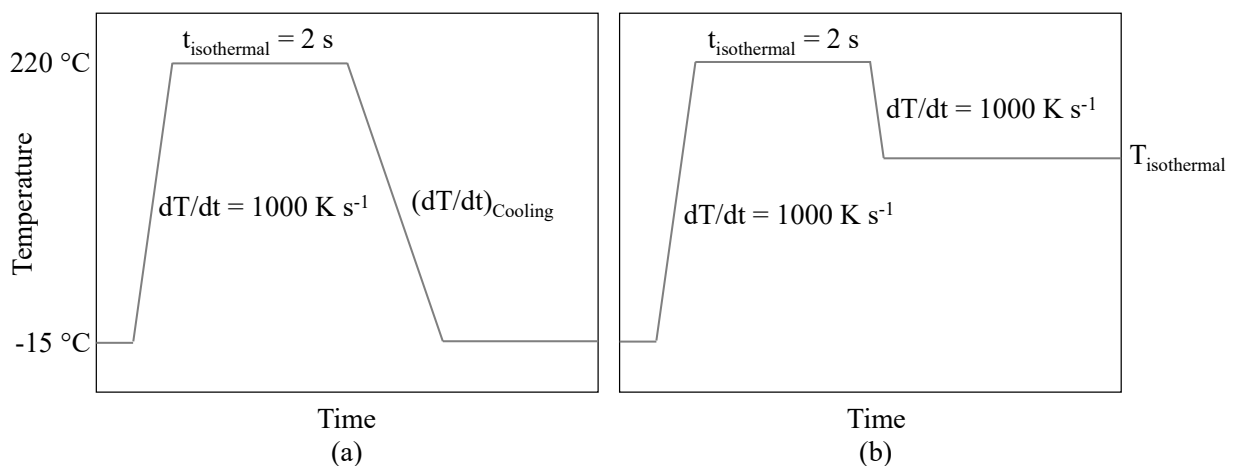


Figure 2. Schematic illustration of temperature–time profiles applied for non-isothermal (a) and isothermal (b) measurements.

In contrast, isothermal measurements were based on a two-step cooling process, corresponding to quenching of the molten polymer by applying a cooling rate of $dT/dt = 1000 \text{ K s}^{-1}$. The subsequent isothermal crystallization step allows for quantifying crystallization kinetics at varied isothermal temperatures in a supercooled state. Table 2 displays the cooling rates of non-isothermal investigations as well as the underlying applied isothermal temperatures that correspond to complementary isothermal investigations.

Table 2. Overview of isothermal and non-isothermal thermal boundary conditions applied to differential scanning calorimetric measurements.

Measurement Mode/-	Isothermal Temperature/ $^{\circ}\text{C}$	Heating Rate/ K s^{-1}
Isothermal	80	-
	90	-
	95	-
	100	-
	105	-
	110	-
	115	-
	120	-
	125	-
	130	-
	135	-
	160	-
	161	-
	162	-
	163	-
	164	-
	165	-
	Non-Isothermal	-
-		60
-		70
-		80
-		90
-		100
-		200
-		300
-		400
-		500
-	1000	
-	2000	

To allow for the complementary thermal characterization of manufactured specimens, non-isothermal differential scanning calorimetry was used to investigate the extent of cold crystallization and temperature-induced relaxations by applying an underlying heating rate of $dT/dt = 60 \text{ K min}^{-1}$.

3.6. Infrared Spectroscopic Analysis

By using samples taken from the center of various tensile specimens as the basis for infrared spectroscopic measurements, the presence of molecular structures that are typical of in situ post condensation reactions were identified. For minimizing the effect of attached powder particles, the skin layer was mechanically removed prior to the measurement. ATR infrared spectroscopy was conducted using a FT-IR device of the type Bruker Invenio FT-IR (Bruker Corporation, Billerica, MA, USA) by applying a wavelength resolution of 0.5 cm^{-1} within a spectral range from $\nu = 400 \text{ cm}^{-1}$ to 4000 cm^{-1} .

4. Results and Discussion

4.1. Isothermal and Non-Isothermal Crystallization Kinetics of Polyamide 12

Process-oriented measurements, based on fast scanning calorimetry of PA12, show a significant supercooling at high cooling rates. In addition to the clear inverse relationship between the crystallization peak temperature and the underlying cooling rate, a growing suppression of crystallization processes is observed, evident in Figure 3. These findings are consistent with those made by Zhang et al. (2022) [27], who concluded that the crystallization of polyamide 12 was predominantly suppressed at cooling rates exceeding 300 K s^{-1} .

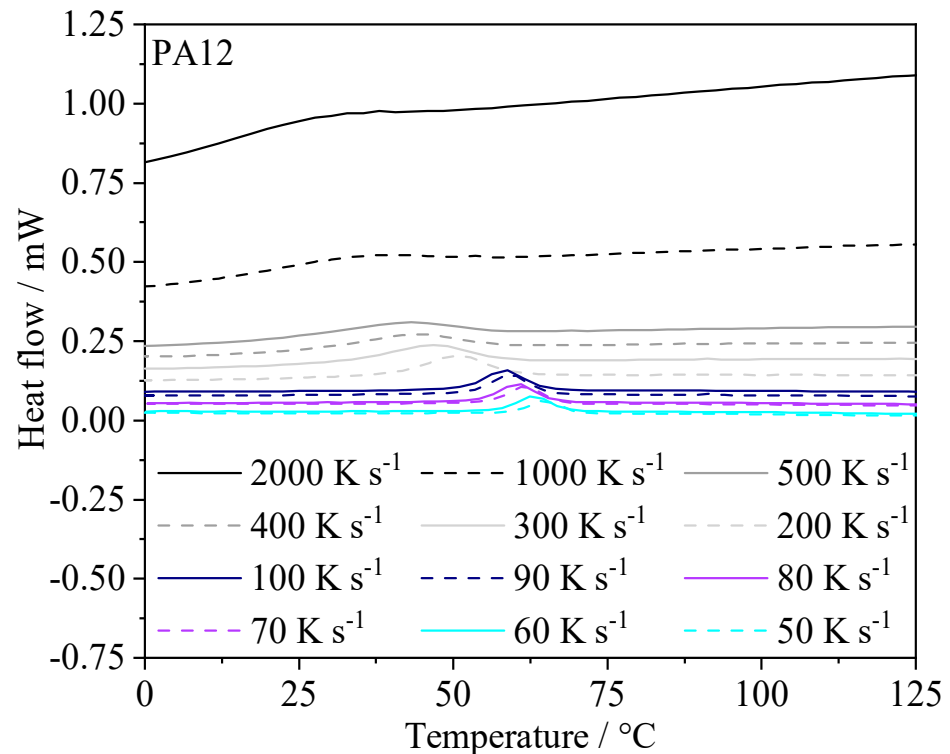


Figure 3. Fast scanning calorimetric measurements of Polyamide 12 at varied, constant cooling rates.

While the qualitative analysis of time-dependent crystallization kinetics is made possible by non-isothermal FSC measurements, the assumption of constant cooling rates is constrained by the temporal decrease of cooling rates that result from LPBF of polymers. Therefore, isothermal FSC and complementary isothermal DSC measurements are considered to obtain indications of the influence of thermal boundary conditions on resulting temperature-dependent isothermal crystallization kinetics.

Consistent with earlier research on isothermal crystallization kinetics of polyamide 12 described by Paolucci et al. (2018) [22], the determined crystallization half times, shown in Figure 4, depict a bimodal distribution of crystallization half times, exhibiting a local maximum at $100 \text{ }^\circ\text{C}$.

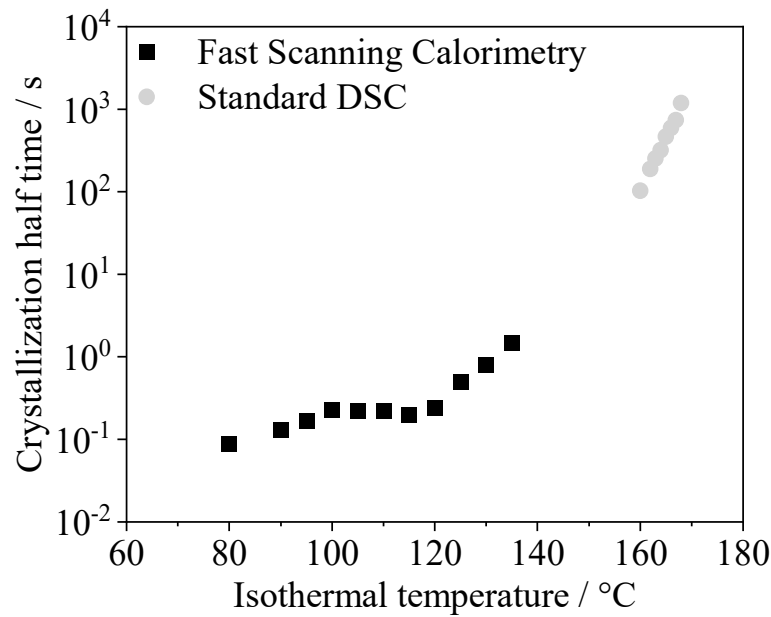


Figure 4. Correlation of isothermal crystallization temperatures and corresponding crystallization kinetics.

4.2. Thermographic In Situ Investigation of Emerging Temperature Fields

Based on the application of quasi-simultaneous, fractal laser exposure, the exposure process depicts a step-wise temperature increase of distinct segments, displayed in Figure 5. Observed peak temperatures depict a positive correlation with the underlying exposure time, exhibiting a near-linear influence of the exposure time and resulting peak temperatures.

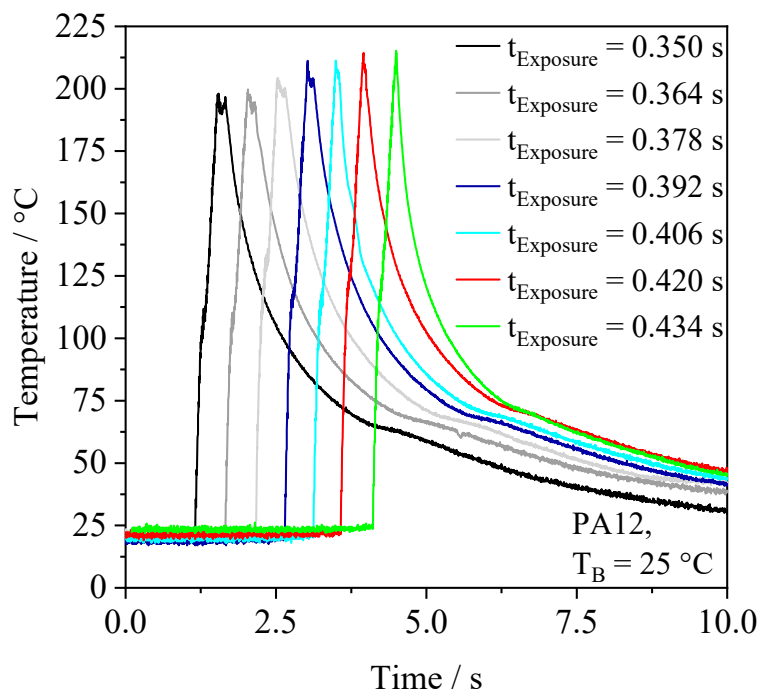


Figure 5. Thermal parameter-dependent process characteristics of fractal, quasi-simultaneous exposure of PA12 at non-isothermal processing conditions.

In contrast to quasi-isothermal LPBF, non-isothermal LPBF is characterized by the vastly accelerated cooling and the corresponding accelerated crystallization of formed polymer melts. A significant temporal contraction of the cooling process is associated with the

emergence of supercooling, consistent with prior fast scanning calorimetric measurements, and semi-empirical models derived from empirical fittings of the Hoffman–Lauritzen theory [24,26], indicating both a reduced crystallization temperature [22] and reduced crystallization half times [22,24]. Given a considerably accelerated crystallization process, high-speed thermal imaging of the cooling process enables the in situ characterization of the exothermal material crystallization based on noticeably increased crystallization kinetics emerging at process-related conditions. Subsequent to the parameter-dependent, rapid cooling of the molten polymer, a parameter-dependent temporary decrease of the thermographically detected cooling rate is observed. A similar phenomenon is evident in quasi-isothermal LPBF of polymers, depicting a slowed cooling induced by material crystallization, determined based on numerical simulations [29]. Figure 6a illustrates the relationship between the calculated non-monotonic variations of the cooling rate and the parameter-dependent exothermal crystallization. Observed time–temperature profiles indicate a positive dependence of the thermographically observed crystallization peak temperature on the underlying quasi-simultaneous exposure time. Figure 6b shows the corresponding definition of the thermographically represented crystallization peak and onset, enabling the reproducible definition of temporal references.

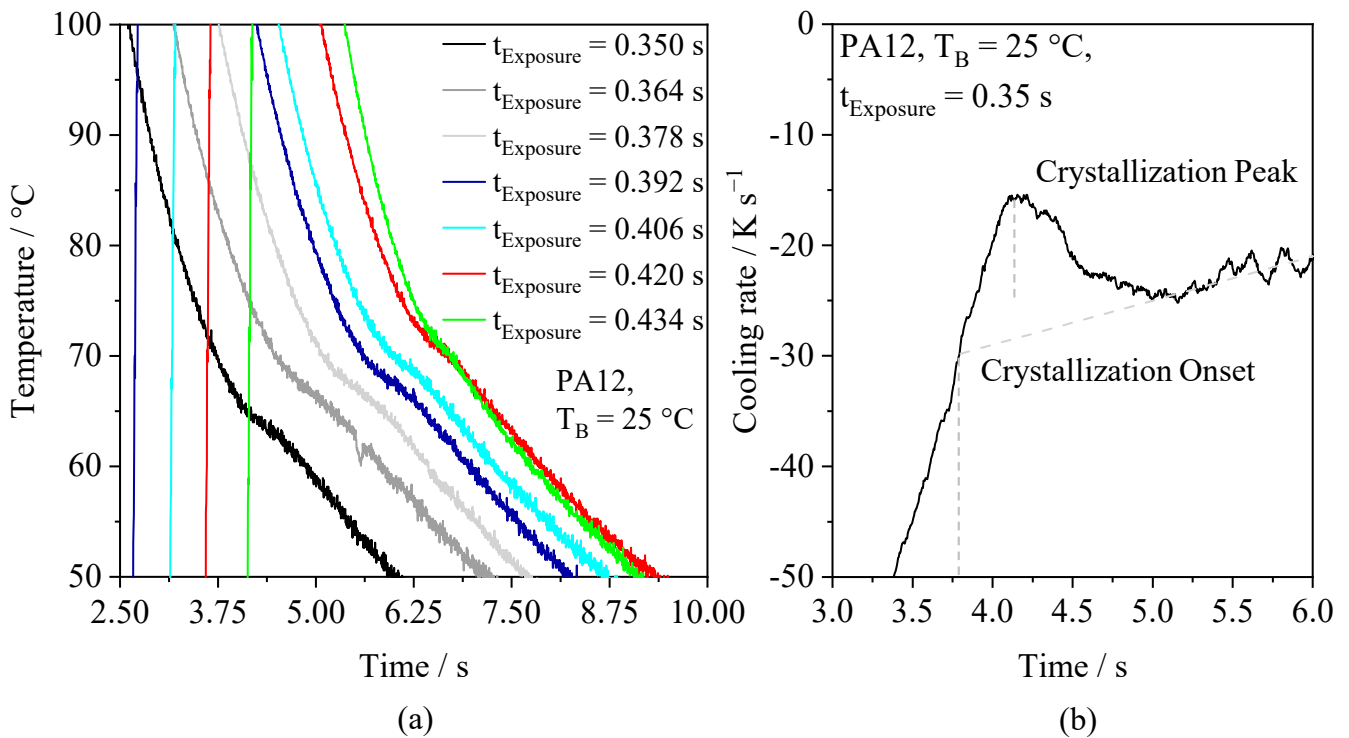


Figure 6. (a) Interdependence of processing parameters and resulting thermal process properties, depicting thermographically represented exothermal crystallization processes; (b) exemplary temporal cooling rate variation, $t_{\text{smoothing}} = 25$ ms.

By considering the temporal variation of the thermographically observable, process-specific temperature derivative, structural process-induced influences on the temporal development of emerging cooling rates are derived. Based on these observations, the peak cooling rate depicts a statistically significant positive correlation ($n = 5$) with the applied effective exposure time, displayed in Figure 7.

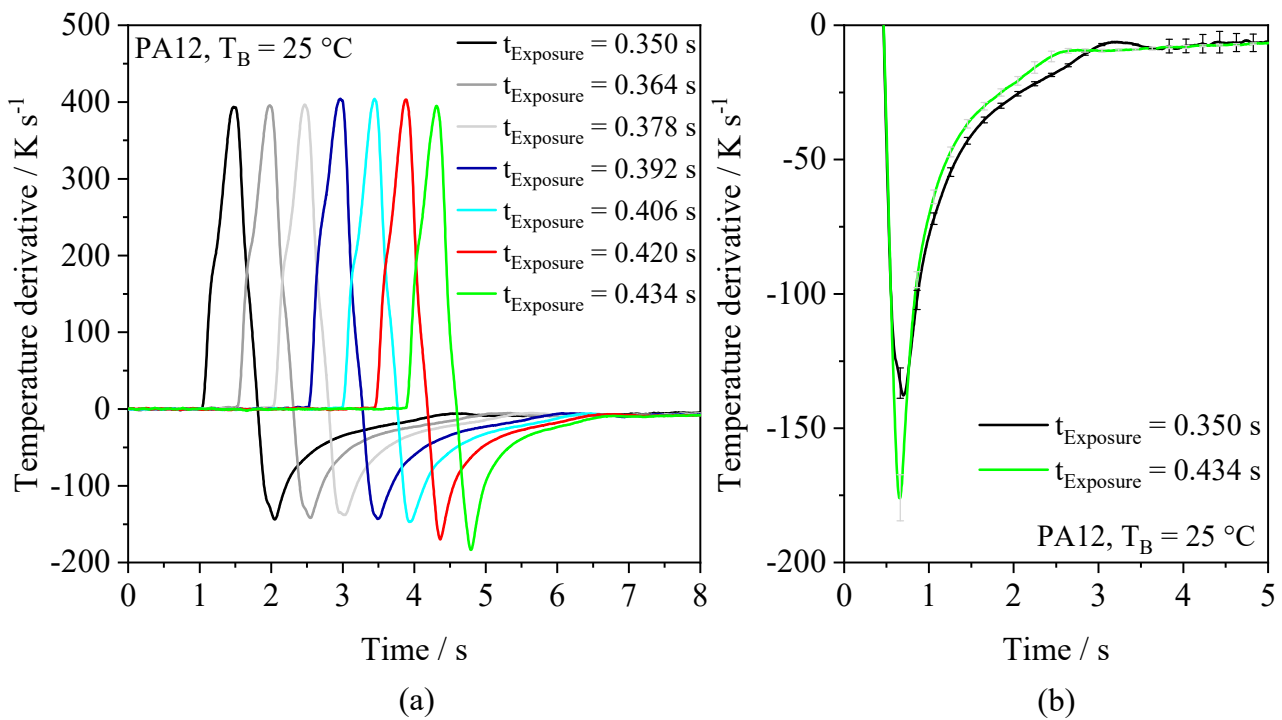


Figure 7. Overview of the part-specific temperature derivative depending on the underlying exposure time in sequential order (a) and normalized in time (b), $t_{\text{Smoothing}} = 25$ ms.

The aforementioned positive correlation of the exposure time and the emerging crystallization peak temperature, displayed in Figure 6, can be correlated with the time-dependent occurrence of process-specific cooling rates. An increased exposure time is correlated with an increased peak cooling rate, followed by a rapid decay of observed cooling rates and a subsequent steady decline of observed cooling rates. The apparent dual-phase process, observed when applying elevated energy density levels, leads to the initial rapid supercooling of the polymer melt. Initiated by the subsequent phase of relatively slow cooling, the crystallization process is observed to occur at an elevated temperature level in accordance with corresponding differential calorimetry measurements. The initial occurrence of elevated cooling rates, evident in Figure 7, is assumed to rely on the extent of thermal conduction into the solid component, based on the assumption of an enhanced inter-layer-bonding and a corresponding increased thermal conductivity of specimens manufactured using increased exposure times. The subsequent decrease of cooling rates observed for shorter exposure times is associated with the influence of elevated exposure times on the thermal penetration depth [38], yielding elevated temperature levels in the solidified part sections, which inhibits the preceding rapid cooling. Figure 8 displays a non-linear relationship between the applied exposure time and the corresponding crystallization peak temperature, consistent with the observed emergence of parameter-dependent cooling rates. A quantitative comparison of thermographically observed crystallization kinetics, and non-isothermal and isothermal measurements using fast scanning calorimetry depicts structural limitations. Temporal data, depicted in Figure 7, indicate a merely negligible influence of cooling rates, occurring immediately after the laser exposure, on the crystallization peak temperature. In contrast, the influence of comparably low cooling rates, observed prior to the material crystallization, depicts a correlation of accelerated cooling and a reduced crystallization temperature. Given the temporal emergence of considerably reduced cooling rates prior to the material crystallization, a qualitative comparison with isothermal FSC measurements portrays considerably increased crystallization half times observed by thermographic measurements.

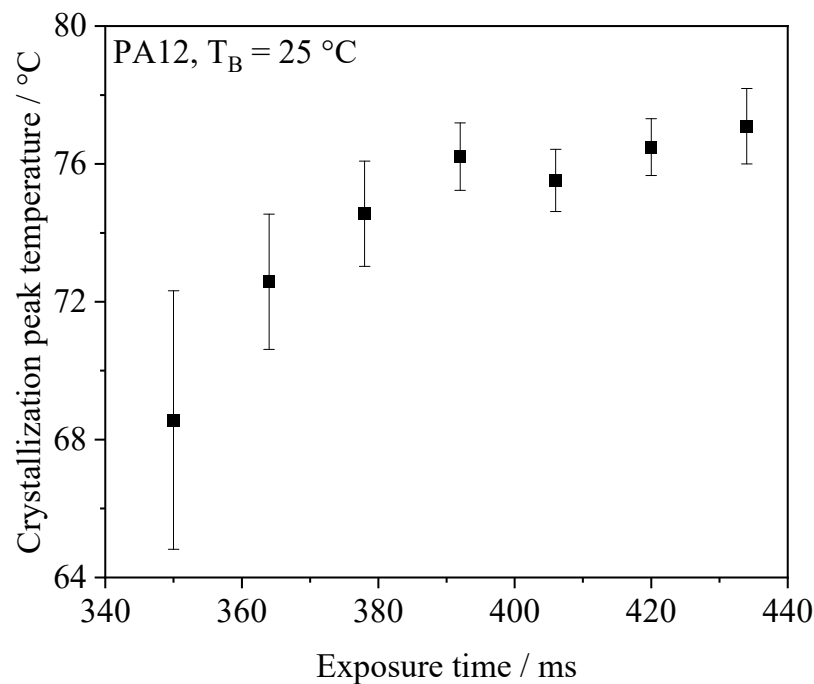


Figure 8. Overview of the parameter dependency of in situ assessed crystallization peak temperatures.

A spatially inhomogeneous crystallization is thought to be responsible for such discrepancies between in situ measurements and ex situ measurements. This indicates that the solid-melt interface represents the initiation point of crystallization due to nucleating effects and heat conduction into the solid material, hence influencing the crystallization half time observed by means of superficial thermographic measurements.

To corroborate discussed interpretations regarding the parameter-dependent emergence of locally varying temperature fields, microscopic investigations are conducted to allow for the correlation of thermographic in situ measurements and corresponding microstructural properties.

4.3. Process-Dependency of Microstructural Properties

Microstructural characteristics of manufactured specimens are significantly influenced by the underlying exposure time and corresponding varying thermal processing properties. Shown in Figure 9, a correlation between the extent of the optically visible, micro-spherulitic phase and the corresponding exposure time suggests an impact on process-dependent crystallization kinetics on the microstructure of emerging parts. Considering the process-dependent crystallization kinetics, elevated crystallization temperatures represent a prerequisite for the formation of micro-spherulitic phases in contrast to the formation of optically amorphous phases, formed at lower crystallization temperatures. However, observed heterogeneous part morphologies indicate a complex interdependence of applied processing parameters and resulting part morphologies.

The formation of both micro-spherulitic and optically amorphous phases in a particular layer is assumed to rely on the occurrence of locally varying cooling rates, being in accordance with a thermographically observed broad thermal crystallization range. A further indication of the influence of melt pool boundaries on the nucleation of discrete agglomerations of optically amorphous and micro-spherulitic phases is the implicit promotion of the observed heterogeneous microstructures and the occurrence of nano-spherulitic layer boundaries. Therefore, the assumed formation of a temperature gradient perpendicular to the powder bed plane is supported by the recurring formation of optically amorphous sections.

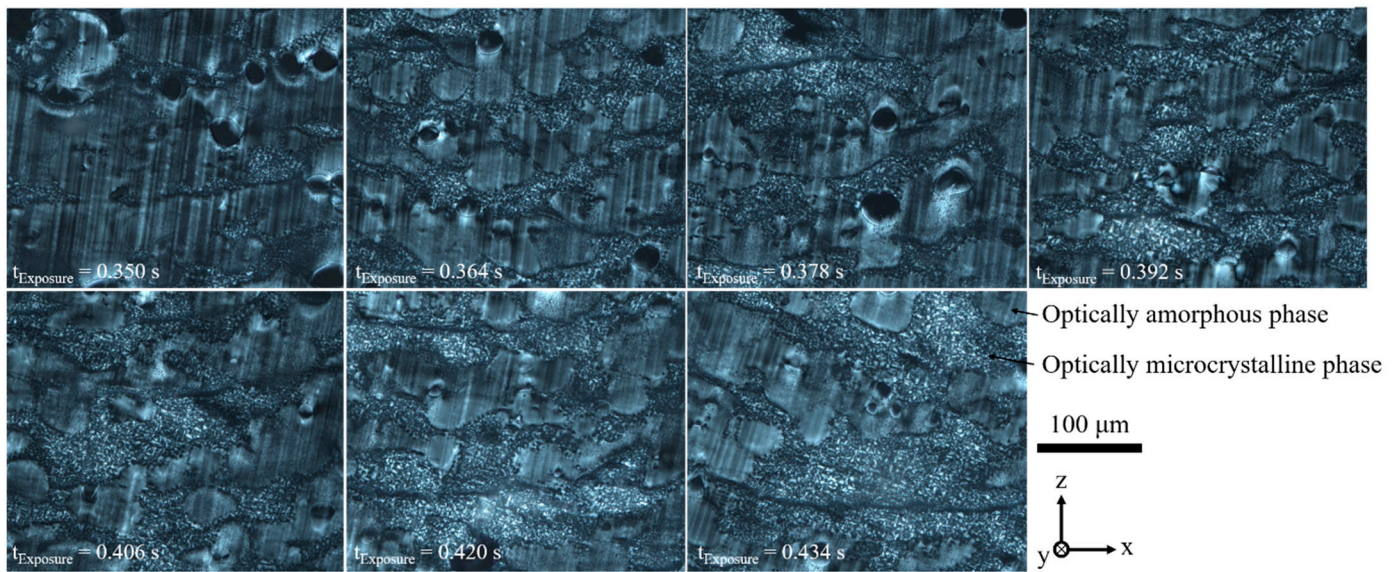


Figure 9. Polarization micrographs depicting the process-dependent formation of microstructural part properties.

In addition to the process-dependent formation of distinct crystalline superstructures, process-dependent temperature fields are correlated with the formation of characteristic patterns of the distribution of pores, determined by means of computed tomography, displayed in Figure 10. The formation of pores depicts a considerable influence of the underlying exposure time, indicating a correlation of increased segment-specific exposure times and the formation of pores in the center of the exposed cross section. In contrast, when applying reduced energy density levels, a bimodal spatial porosity distribution can be observed, indicating the occurrence of merely low levels of porosity on the edge area. The underlying segment-specific exposure time depicts a non-linear correlation with the corresponding part porosity, exhibiting a sudden increase towards a considerable extent of central pores when exceeding an exposure time of 0.392 s, depicting a pronounced trimodal distribution. A further increase of the exposure time is associated with the less pronounced concentration of pores in the part center, depicting a reduction of centralized porosity, suggesting an influence of thermal degradation and improved material coalescence as opposite effects on central part porosity. The influence of improved material coalescence is assumed to be associated with increased peak temperatures, corresponding to a reduced melt viscosity as well as an increased timespan available for material coalescence. Furthermore, regardless of varying porosity levels in the center of manufactured parts, a positive correlation of the applied energy density and the occurrence of porosity near the edge region can be observed, associated with increased peak temperatures.

In addition to the implicit representation of exposure parameters with regard to occurring porosity, further influences of the exposure time can be identified concerning the fracture surface, exhibiting a positive correlation of brittle fracture surfaces and the underlying quasi-simultaneous exposure time, displayed in Figure 11. Observed fracture surfaces exhibit a correlation of ductile material properties and the microscopically observed extent of optically amorphous material phases, indicating an influence of formed crystalline superstructures on part failure properties.

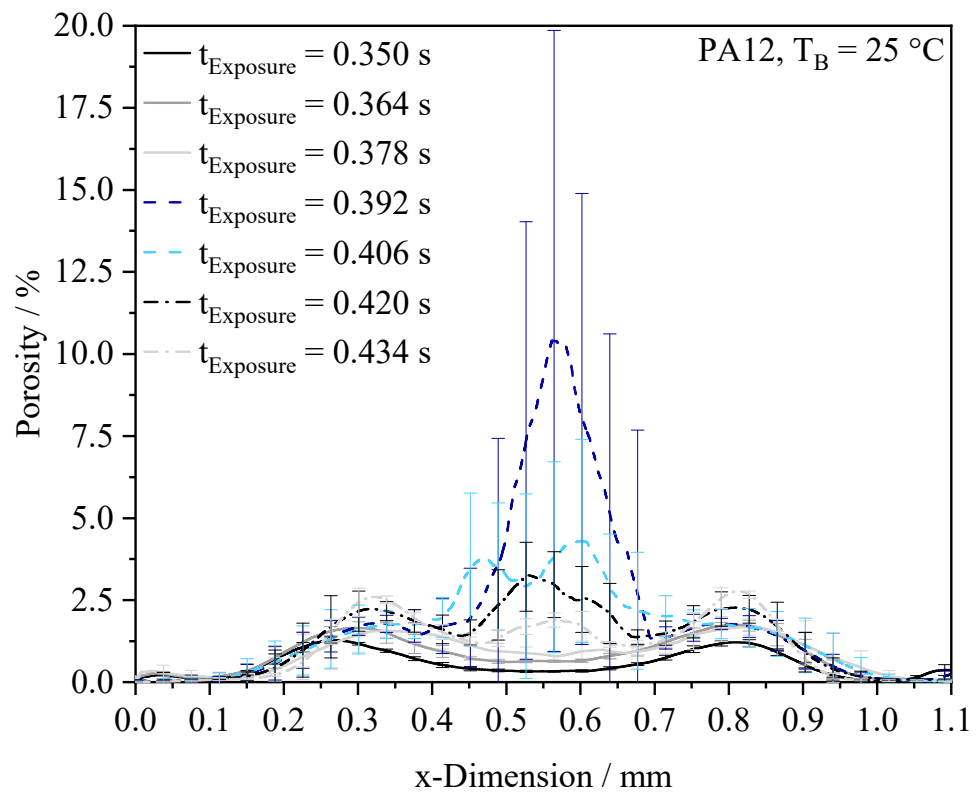


Figure 10. Spatial distribution of pores contingent on the applied segment-specific exposure time, $n = 5$.

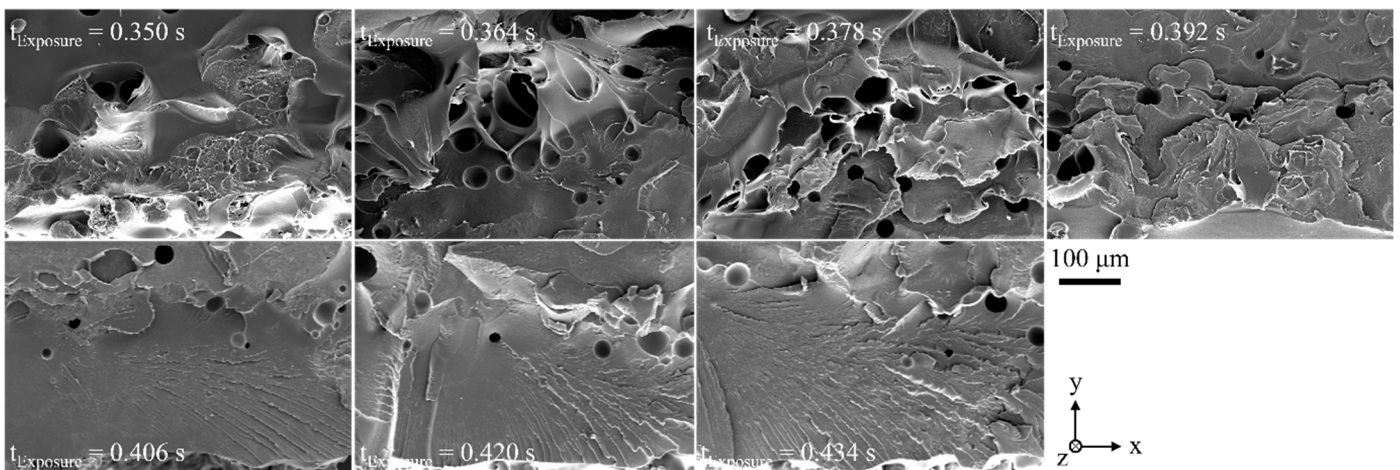


Figure 11. Scanning electron micrographs of fracture surfaces depending on the underlying exposure time.

With regard to the observed surface topology, further significant effects of applied processing parameters on the superficial roughness of manufactured samples can be observed by means of laser scanning microscopy, displayed in Figure 12.

Increasing quasi-simultaneous exposure times are negatively correlated with the part surface roughness, indicating the enhanced consolidation of adhering particles influenced by an increased energy input level and accordingly increased exposure times.

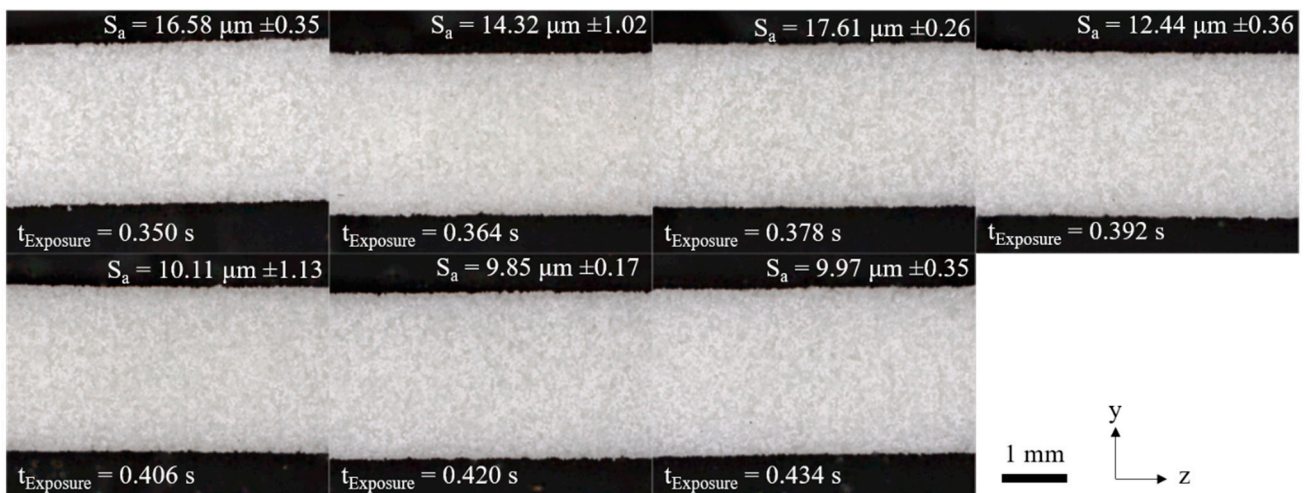


Figure 12. Combined optical and confocal laser scanning imaging of the surface topology of manufactured tensile specimens.

4.4. Interdependencies of Mechanical and Process Properties

In addition to observed microstructural variations, associated with specific thermal processing properties and varying crystallization kinetics, influences on emerging mechanical part properties can be derived. Observed mechanical properties depict a structural influence of the applied exposure time on the failure behavior of manufactured specimens, displayed in Figure 13, leading to an enhanced elongation at break while minimizing the required exposure time. A significantly reduced tensile strength is observed when utilizing thin-walled geometries with a cross section of $A = 2.5 \text{ mm}^2$ and the applied build orientation, regardless of the processing parameters used. These observations are in accordance with findings by Sindinger et al. [39,40] regarding quasi-isothermal LPBF, describing significant reductions of both the tensile strength and the elongation at break of thin-walled specimens of tensile specimens built perpendicular to the powder bed plane, associated with significantly impaired failure properties. Furthermore, the interdependence of morphological and corresponding mechanical properties indicates the correlation of the extent of the optically amorphous phase and the elongation at break. An increased variance of the elongation at break observed for reduced exposure times is assumed to partially rely on the statistical occurrence of defects, such as insufficient inter-layer bonding, and is associated with the build orientation of manufactured tensile specimens. However, the elongation at break does not depict a correlation with the respective surface roughness of manufactured specimens, indicating an effect of microstructural properties on the observed mechanical variations, in accordance with corresponding observed morphological alterations regarding the occurrence of centralized porosity and nano-spherulitic microstructures.

The non-linear dependency of the underlying exposure time and emerging crystallization peak temperature, discussed previously, depicts a correlation with an interdependence of the crystallization temperature and the elongation at break. Therefore, the influence of processing parameters is correlated with the formation of varying temperature fields, leading to adapted microstructural material properties, and varying mechanical properties. The process-dependent formation of nano-spherulitic microstructures is assumed to contribute to the enhancement of the failure properties alongside a minimized level of part porosity. Therefore, the considerable dependency of resulting mechanical part properties and underlying thermal process characteristics implies the potential for further process-related enhancements.

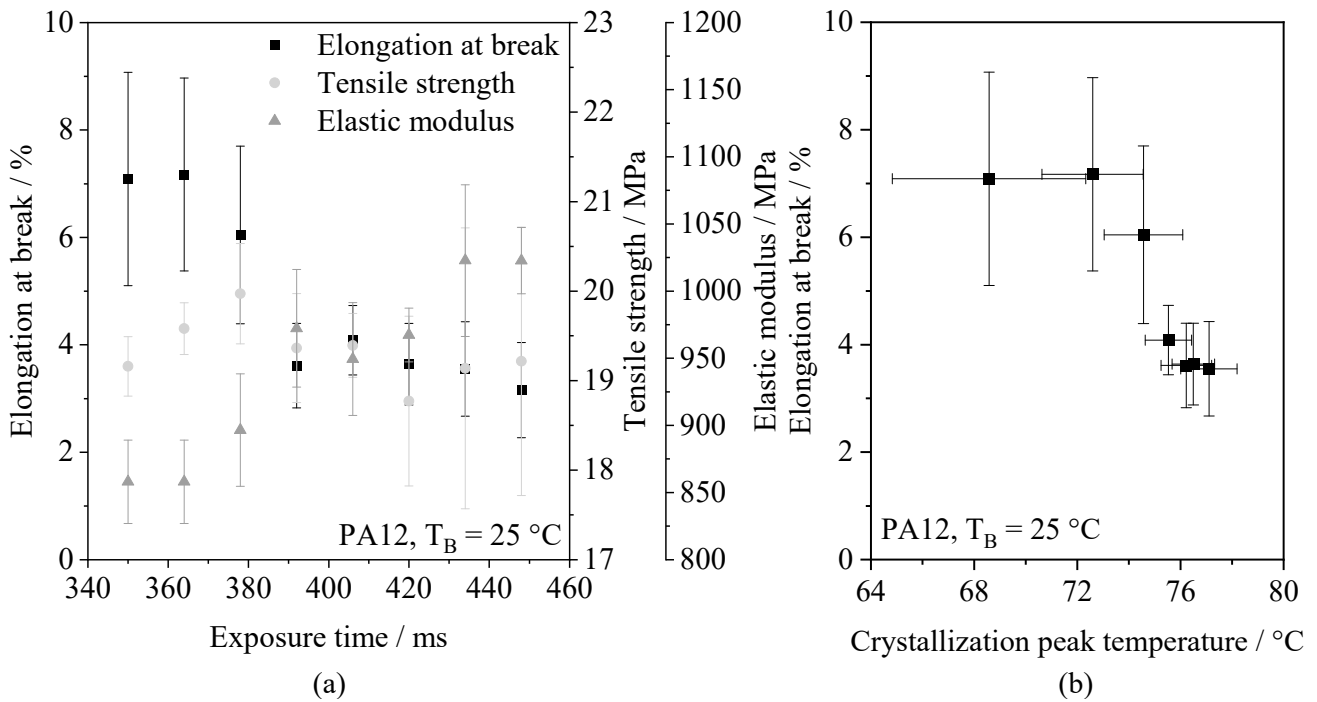


Figure 13. Overview of resulting mechanical properties depending on processing parameters (a), and relative to in situ assessed crystallization peak temperatures (b), $n = 5$.

4.5. Process-Dependency of Thermal and Thermo-Mechanical Material Characteristics

The occurrence of elevated cooling rates, observed in situ using thermographic imaging, is correlated with the emergence of thermally induced post crystallization of metastable phase compositions [22,23,41]. By applying non-isothermal differential scanning calorimetry, the occurrence of cold crystallization can be identified. Figure 14 illustrates merely negligible effects of varying processing conditions on the degree of cold crystallization with respect to the previously discussed process-dependent morphological variability.

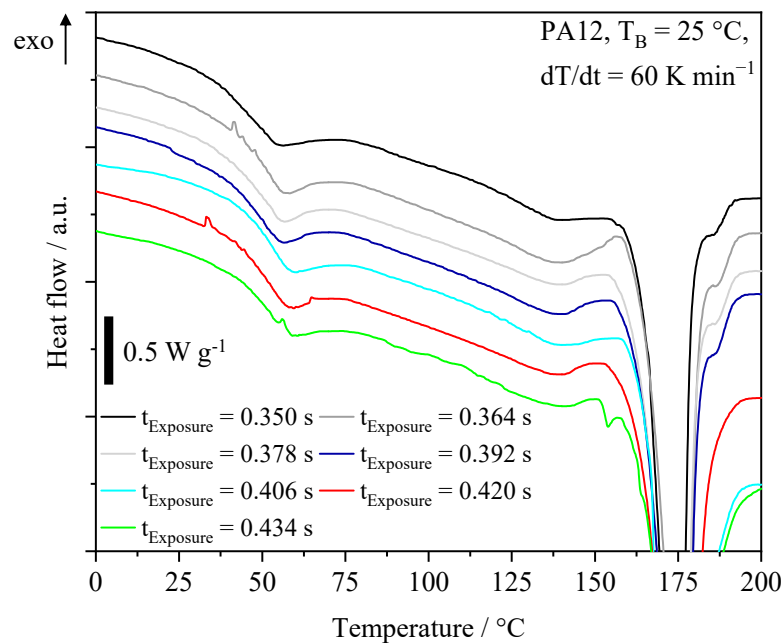


Figure 14. Differential scanning calorimetric measurements of manufactured specimens depending on underlying processing parameters.

In contrast to the aforementioned morphologically represented dual-phase composition of micro-spherulitic and optically amorphous phases, observed thermal properties of manufactured specimens do not corroborate the formation of a dual-phase morphology. Instead, thermal investigations indicate the formation of nanoscopic crystalline structures, not detectable by means of light microscopy in the visual spectrum. In accordance with findings by Fischer et al. (2017) [42], the formation of nano-crystalline structures is correlated with adapted mechanical failure properties, describing both a reduced tensile strength and an increased elongation at break at reduced crystallization temperatures, consistent with observed mechanical properties. Based on complementary dynamic-mechanical characterizations, no significant influences of varied exposure times on temperature-dependent dynamic mechanical properties are derived, as seen in Figure 15.

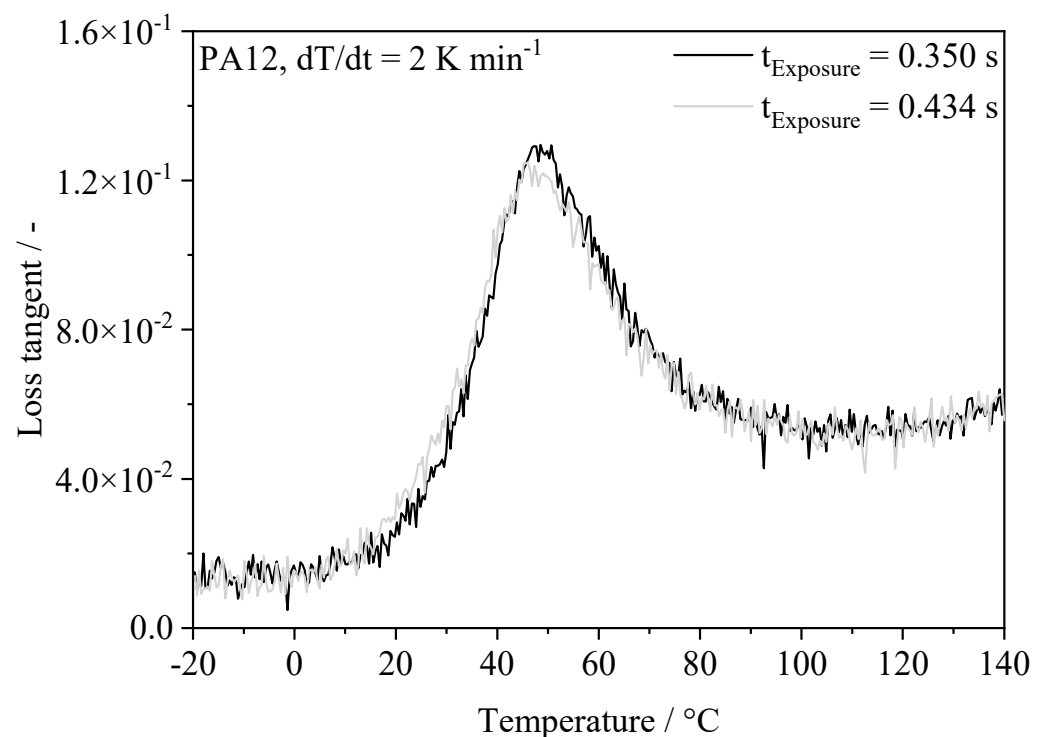


Figure 15. Temperature-dependency of the loss tangent of manufactured tensile specimens.

These observations are consistent with aforementioned thermal properties, displaying no significant influence of applied exposure parameters on the extent of phase changes. Considering the process-specific formation of meta-stable phase compositions determined by means of DSC, complementary infrared spectroscopic measurements indicate the formation of a combined ($\alpha + \gamma$)-phase, derived from the fingerprint region [43–46].

Displayed in Figure 16, ATR-FTIR measurements of manufactured specimens depict distinct peaks at 577 cm^{-1} and 626 cm^{-1} , corresponding to the Amide VI band, and are associated with the formation of the α -phase and the γ -phase, respectively [44–46]. Despite structural similarities of determined FTIR spectra, qualitative differences of the absorption peaks indicate the facilitated formation of absorption peaks attributed to the α -phase. These differences, induced by reduced exposure times, are correlated with an increased extent of supercooling. Furthermore, a shift towards an increased frequency, observed for the 577 cm^{-1} peak, is correlated with reduced crystallization peak temperatures. In addition to explaining thermal material properties, the identified phase composition is correlated with a reduced Young's modulus and a reduced tensile strength of fabricated tensile specimens [46]. Although thermographic observations suggest the intermediate formation of mesomorphic fractions given the observed crystallization temperatures [22,47], the thermal history of distinct layers suggests the occurrence of cold crystallization of

metastable fractions induced by repeated heating due to the exposure of subsequent layers. Consequently, given the thin-walled part cross section, experimental findings indicate a superposition of geometric influences [39] and the present polymorphism of polyamide 12 on emerging mechanical properties.

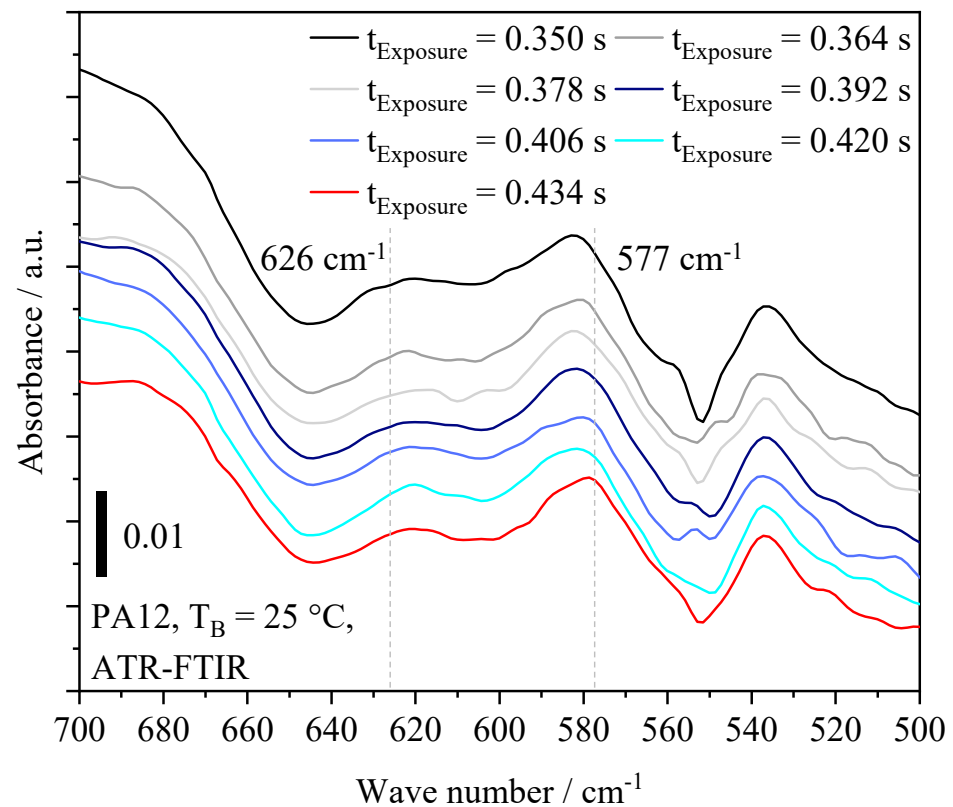


Figure 16. Infrared spectrum of tensile specimens depending on underlying processing parameters.

5. Conclusions

Within the present research, the non-isothermal, support-free powder-based additive manufacturing of thin-walled components is demonstrated. Underlying exposure strategies applied for the non-isothermal processing of polyamide 12 are characterized by the implicit temporal and spatial discretization of the melting and subsequent crystallization, relying on quasi-simultaneous exposure of distinct segments. Based on the exposure-based modification of thermal processing conditions, interdependencies between processing parameters, resulting temperature fields and corresponding emergent mechanical, microstructural, and thermal part properties are derived. By applying thermographic process analysis, process-dependent crystallization kinetics are determined in situ based on the exothermic nature of crystallization processes, hence temporarily inhibiting the cooling process. An increase of the segment-specific thermal exposure time is correlated with an increased thermal penetration, implicitly affecting the formation of micro-spherulitic structures. In contrast, limiting the thermal exposure of distinct segments allows for promoting the formation of an optically amorphous phase. Using infrared spectroscopic analysis, the formation of the $(\alpha + \gamma)$ -phase is derived in accordance with the observed adapted mechanical and thermal part properties, depicting post crystallization of metastable phase compositions. Based on complementary thermal and thermo-mechanical investigations, improved failure properties are partially associated with the formation of microscopically observed, nanoscopic crystalline structures, while no significant influences of processing parameters on thermo-mechanical properties are identified.

As a result, time-dependent processing parameters enable the control of emergent part properties, serving as a basis for the exposure-based, local adaptation of macroscopic

and microscopic properties to specific local applications. Given the complexity of process-morphology-mechanics interdependencies, future research will focus on the controlled, locally varying modification of part properties, allowing for significantly extending the range of accessible material properties in LPBF of polymers. Furthermore, interdependencies of non-isothermal processing conditions and the formation of metastable material modifications are of great interest for future research, indicating the requirement for adapting transient thermal boundary conditions of the crystallization step.

Author Contributions: Conceptualization, Methodology, Formal Analysis, Software, Validation, and Writing—Initial Draft: S.S., Investigations S.S. and S.C., Writing—Review and Editing: S.C., Funding Acquisition, Supervision and Project Administration: D.D. All authors have read and agreed to the published version of the manuscript.

Funding: Funded by the Deutsche Forschungsgemeinschaft (DFG, German Research Foundation) Project-ID 61375930 SFB 814—“Additive Manufacturing” TP A03 and TP B03.

Data Availability Statement: The data presented in this study are not publicly available due to ongoing research in this field.

Conflicts of Interest: The authors declare no conflict of interest.

References

1. Wudy, K.; Drummer, D. Aging effects of polyamide 12 in selective laser sintering: Molecular weight distribution and thermal properties. *Addit. Manuf.* **2018**, *25*, 1–9. [[CrossRef](#)]
2. Wudy, K.; Drummer, D.; Kuhnlein, F.; Drexler, M. Influence of degradation behavior of polyamide 12 powders in laser sintering process on produced parts. *AIP Conf. Proc.* **2014**, *1593*, 691–695. [[CrossRef](#)]
3. Lanzl, L.; Wudy, K.; Drummer, D. The effect of short glass fibers on the process behavior of polyamide 12 during selective laser beam melting. *Polym. Test.* **2020**, *83*, 106313. [[CrossRef](#)]
4. Schlicht, S.; Greiner, S.; Drummer, D. Low Temperature Powder Bed Fusion of Polymers by Means of Fractal Quasi-Simultaneous Exposure Strategies. *Polymers* **2022**, *14*, 1428. [[CrossRef](#)]
5. Kigure, T.; Yamauchi, Y.; Niino, T. Relationship between powder bed temperature and microstructure of laser sintered PA12 parts. In *2019 International Solid Freeform Fabrication Symposium*; University of Texas at Austin: Austin, TX, USA, 2019.
6. Niino, T.; Haraguchi, H.; Itagaki, Y.; Hara, K.; Morita, S. Microstructural observation and mechanical property evaluation of plastic parts obtained by preheat free laser sintering. In *2012 International Solid Freeform Fabrication Symposium*; University of Texas at Austin: Austin, TX, USA, 2012; pp. 617–628.
7. Drexler, M.; Lexow, M.; Drummer, D. Selective Laser Melting of Polymer Powder—Part Mechanics as Function of Exposure Speed. *Phys. Procedia* **2015**, *78*, 328–336. [[CrossRef](#)]
8. Greiner, S.; Wudy, K.; Wörz, A.; Drummer, D. Thermographic investigation of laser-induced temperature fields in selective laser beam melting of polymers. *Opt. Laser Technol.* **2018**, *109*, 569–576. [[CrossRef](#)]
9. Wegner, A.; Witt, G. Process monitoring in laser sintering using thermal imaging. In *2011 International Solid Freeform Fabrication Symposium*; University of Texas at Austin: Austin, TX, USA, 2011.
10. Zou, S.; Xiao, H.; Ye, F.; Li, Z.; Tang, W.; Zhu, F.; Chen, C.; Zhu, C. Numerical analysis of the effect of the scan strategy on the residual stress in the multi-laser selective laser melting. *Results Phys.* **2020**, *16*, 103005. [[CrossRef](#)]
11. Pavan, M.; Faes, M.; Strobbe, D.; Van Hooreweder, B.; Craeghs, T.; Moens, D.; Dewulf, W. On the influence of inter-layer time and energy density on selected critical-to-quality properties of PA12 parts produced via laser sintering. *Polym. Test.* **2017**, *61*, 386–395. [[CrossRef](#)]
12. Shi, Q.; Gu, D.; Xia, M.; Cao, S.; Rong, T. Effects of laser processing parameters on thermal behavior and melting/solidification mechanism during selective laser melting of TiC/Inconel 718 composites. *Opt. Laser Technol.* **2016**, *84*, 9–22. [[CrossRef](#)]
13. Li, Y.; Gu, D. Thermal behavior during selective laser melting of commercially pure titanium powder: Numerical simulation and experimental study. *Addit. Manuf.* **2014**, *1*, 99–109. [[CrossRef](#)]
14. Zhang, D.; Zhang, P.; Liu, Z.; Feng, Z.; Wang, C.; Guo, Y. Thermofluid field of molten pool and its effects during selective laser melting (SLM) of Inconel 718 alloy. *Addit. Manuf.* **2018**, *21*, 567–578. [[CrossRef](#)]
15. Chen, C.; Yin, J.; Zhu, H.; Xiao, Z.; Zhang, L.; Zeng, X. Effect of overlap rate and pattern on residual stress in selective laser melting. *Int. J. Mach. Tools Manuf.* **2019**, *145*, 103433. [[CrossRef](#)]
16. Parry, L.; Ashcroft, I.; Wildman, R. Understanding the effect of laser scan strategy on residual stress in selective laser melting through thermo-mechanical simulation. *Addit. Manuf.* **2016**, *12*, 1–15. [[CrossRef](#)]
17. Catchpole-Smith, S.; Aboulkhair, N.; Parry, L.; Tuck, C.; Ashcroft, I.; Clare, A. Fractal scan strategies for selective laser melting of ‘unweldable’ nickel superalloys. *Addit. Manuf.* **2017**, *15*, 113–122. [[CrossRef](#)]

18. Greiner, S.; Schlicht, S.; Drummer, D. Temperature field homogenization by fractal exposure strategies in laser sintering of polymers. In Proceedings of the 17th Rapid.Tech 3D Conference, Erfurt, Germany, 22–23 June 2021; Carl Hanser Verlag GmbH & Co.: München, Germany, 2021; pp. 188–197.
19. Drummer, D.; Greiner, S.; Zhao, M.; Wudy, K. A novel approach for understanding laser sintering of polymers. *Addit. Manuf.* **2019**, *27*, 379–388. [[CrossRef](#)]
20. Soldner, D.; Greiner, S.; Burkhardt, C.; Drummer, D.; Steinmann, P.; Mergheim, J. Numerical and experimental investigation of the isothermal assumption in selective laser sintering of PA12. *Addit. Manuf.* **2020**, *37*, 101676. [[CrossRef](#)]
21. Soldner, D.; Steinmann, P.; Mergheim, J. Modeling crystallization kinetics for selective laser sintering of polyamide 12. *Gamm-Mitteilungen* **2021**, *44*, e202100011. [[CrossRef](#)]
22. Paolucci, F.; Baeten, D.; Roozmond, P.; Goderis, B.; Peters, G. Quantification of isothermal crystallization of polyamide 12: Modelling of crystallization kinetics and phase composition. *Polymer* **2018**, *155*, 187–198. [[CrossRef](#)]
23. Paolucci, F.; van Mook, M.; Govaert, L.; Peters, G. Influence of post-condensation on the crystallization kinetics of PA12: From virgin to reused powder. *Polymer* **2019**, *175*, 161–170. [[CrossRef](#)]
24. Zhao, M.; Wudy, K.; Drummer, D. Crystallization Kinetics of Polyamide 12 during Selective Laser Sintering. *Polymers* **2018**, *10*, 168. [[CrossRef](#)]
25. Greiner, S.; Jaksch, A.; Cholewa, S.; Drummer, D. Development of material-adapted processing strategies for laser sintering of polyamide 12. *Adv. Ind. Eng. Polym. Res.* **2021**, *4*, 251–263. [[CrossRef](#)]
26. Ren, M.; Mo, Z.; Chen, Q.; Song, J.; Wang, S.; Zhang, H.; Zhao, Q. Crystallization kinetics and morphology of nylon 1212. *Polymer* **2004**, *45*, 3511–3518. [[CrossRef](#)]
27. Zhang, R.; Jariyavidyanont, K.; Du, M.; Zhuravlev, E.; Schick, C.; Androsch, R. Nucleation and crystallization kinetics of polyamide 12 investigated by fast scanning calorimetry. *J. Polym. Sci.* **2021**, *60*, 842–855. [[CrossRef](#)]
28. Amado, A.; Wegener, K.; Schmid, M.; Levy, G. Characterization and modeling of non-isothermal crystallization of Polyamide 12 and co-Polypropylene during the SLS process. In Proceedings of the 5th International Polymers & Moulds Innovations Conference, Ghent, Belgium, 12–14 September 2012.
29. Shen, F.; Zhu, W.; Zhou, K.; Ke, L.-L. Modeling the temperature, crystallization, and residual stress for selective laser sintering of polymeric powder. *Acta Mech.* **2021**, *232*, 3635–3653. [[CrossRef](#)]
30. Niino, T.; Haraguchi, H.; Itagaki, Y. Feasibility study on plastic laser sintering without powder bed preheating. In *2011 International Solid Freeform Fabrication Symposium*; University of Texas at Austin: Austin, TX, USA, 2011; pp. 17–29.
31. Neugebauer, F.; Ploshikhin, V.; Ambrosy, J.; Witt, G. Isothermal and non-isothermal crystallization kinetics of polyamide 12 used in laser sintering. *J. Therm. Anal. Calorim.* **2016**, *124*, 925–933. [[CrossRef](#)]
32. Nakamura, K.; Watanabe, T.; Katayama, K.; Amano, T. Some aspects of nonisothermal crystallization of polymers. I. Relationship between crystallization temperature, crystallinity, and cooling conditions. *J. Appl. Polym. Sci.* **1972**, *16*, 1077–1091. [[CrossRef](#)]
33. Nakamura, K.; Katayama, K.; Amano, T. Some aspects of nonisothermal crystallization of polymers. II. Consideration of the isokinetic condition. *J. Appl. Polym. Sci.* **1973**, *17*, 1031–1041. [[CrossRef](#)]
34. Plummer, C.J.G.; Zanetto, J.-E.; Bourban, P.-E.; Manson, J.-A.E. The crystallization kinetics of polyamide-12. *Colloid Polym. Sci.* **2001**, *279*, 312–322. [[CrossRef](#)]
35. Ehrenstein, G.W.; Theriault, R.P. *Polymeric Materials: Structure, Properties, Applications*; Hanser Publishers: Cincinnati, OH, USA, 2001.
36. Peano, G. Sur une courbe, qui remplit toute une aire plane. *Math. Ann.* **1890**, *36*, 157–160. [[CrossRef](#)]
37. Yang, J.; Bin, H.; Zhang, X.; Liu, Z. Fractal scanning path generation and control system for selective laser sintering (SLS). *Int. J. Mach. Tools Manuf.* **2003**, *43*, 293–300. [[CrossRef](#)]
38. Marín, E. Characteristic dimensions for heat transfer. *Lat. Am. J. Phys. Educ.* **2010**, *4*, 56–60.
39. Sindinger, S.-L.; Kralovec, C.; Tasch, D.; Schagerl, M. Thickness dependent anisotropy of mechanical properties and inhomogeneous porosity characteristics in laser-sintered polyamide 12 specimens. *Addit. Manuf.* **2020**, *33*, 101141. [[CrossRef](#)]
40. Sindinger, S.-L.; Marschall, D.; Kralovec, C.; Schagerl, M. Structural Response Prediction of Thin-Walled Additively Manufactured Parts Considering Orthotropy, Thickness Dependency and Scatter. *Materials* **2021**, *14*, 2463. [[CrossRef](#)] [[PubMed](#)]
41. Verkinderen, O.; Baeten, D.; Van Puyvelde, P.; Goderis, B. The crystallization of PA11, PA12, and their random copolymers at increasing supercooling: From eutectic segregation to mesomorphic solid solutions. *Polym. Cryst.* **2021**, *4*, e10216. [[CrossRef](#)]
42. Fischer, C.; Seefried, A.; Drummer, D. Crystallization and Component Properties of Polyamide 12 at Processing-Relevant Cooling Conditions. *Polym. Eng. Sci.* **2016**, *57*, 450–457. [[CrossRef](#)]
43. Matsubara, I.; Magill, J.H. Lower-frequency infrared spectra and structures of some typical aliphatic polyamides. *J. Polym. Sci. Part A-2: Polym. Phys.* **1973**, *11*, 1173–1187. [[CrossRef](#)]
44. Rhee, S.; White, J.L. Crystal structure and morphology of biaxially oriented polyamide 12 films. *J. Polym. Sci. Part B Polym. Phys.* **2002**, *40*, 1189–1200. [[CrossRef](#)]
45. Han, J.; Cao, Z.; Gao, W. Remarkable sorption properties of polyamide 12 microspheres for a broad-spectrum antibacterial (triclosan) in water. *J. Mater. Chem. A* **2013**, *1*, 4941–4944. [[CrossRef](#)]

46. Ma, N.; Liu, W.; Ma, L.; He, S.; Liu, H.; Zhang, Z.; Sun, A.; Huang, M.; Zhu, C. Crystal transition and thermal behavior of Nylon 12. *E-Polymers* **2020**, *20*, 346–352. [[CrossRef](#)]
47. Cholewa, S.; Drummer, D. Crystallization behavior under process conditions in Powder Bed Fusion of polymers. *Procedia CIRP* **2022**, *111*, 23–27. [[CrossRef](#)]

Disclaimer/Publisher’s Note: The statements, opinions and data contained in all publications are solely those of the individual author(s) and contributor(s) and not of MDPI and/or the editor(s). MDPI and/or the editor(s) disclaim responsibility for any injury to people or property resulting from any ideas, methods, instructions or products referred to in the content.